QUANTUM INFORMATION

Resonantly driven CNOT gate for electron spins

D. M. Zajac,[1] A. J. Sigillito,[1] M. Russ,[2] F. Borjans,[1] J. M. Taylor,[3,4] G. Burkard,[2] J. R. Petta[1]*

Single-qubit rotations and two-qubit CNOT operations are crucial ingredients for universal quantum computing. Although high-fidelity single-qubit operations have been achieved using the electron spin degree of freedom, realizing a robust CNOT gate has been challenging because of rapid nuclear spin dephasing and charge noise. We demonstrate an efficient resonantly driven CNOT gate for electron spins in silicon. Our platform achieves single-qubit rotations with fidelities greater than 99%, as verified by randomized benchmarking. Gate control of the exchange coupling allows a quantum CNOT gate to be implemented with resonant driving in ~200 nanoseconds. We used the CNOT gate to generate a Bell state with 78% fidelity (corrected for errors in state preparation and measurement). Our quantum dot device architecture enables multi-qubit algorithms in silicon.

Gate-defined semiconductor quantum dots are a powerful platform for isolating and coherently controlling single electron spins (*1*, *2*). Silicon quantum dots can take advantage of state-of-the-art industrial nanofabrication capabilities for scalability (*3*), and support some of the longest quantum coherence times measured in the solid state (*4*, *5*). By engineering local magnetic field gradients, electron spins can be electrically controlled (*6*, *7*) with single-qubit gate fidelities exceeding 99.9% (*8*, *9*). Although exchange control of spins was demonstrated as early as 2005 (*10*), demonstrations of two-qubit gates with quantum dot spins are scarce owing to technological and materials challenges (*11*–*14*). A demonstration of an efficient CNOT gate for spins in silicon will open a path for multi-qubit algorithms in a scalable semiconductor system.

Here, we demonstrate a ~200-ns CNOT gate in a silicon semiconductor double quantum dot (DQD), nearly an order of magnitude faster than the previously demonstrated composite CNOT gate (*14*). Turning on an exchange interaction results in a state-selective electron spin resonance (ESR) transition that is used to implement a CNOT gate with a single microwave (MW) pulse. Unlike previous DQD implementations of the exchange gate, our CNOT gate is implemented at a symmetric operating point, where the exchange coupling J is first-order insensitive to charge noise (*15*–*17*).

We use the spin of a single electron to encode a qubit (*18*). A gate-defined DQD (Fig. 1A) isolates two electrons in a silicon quantum well with natural isotopic abundance, forming a two-qubit device (Fig. 1B). Gates L and R are used to control the energy of the electrons trapped in the left and right quantum dots, respectively, and gate M provides control of J. The charge occupancy of the DQD is detected by monitoring the current I_S or conductance g_S through a nearby quantum dot charge sensor (*19*). A Co micromagnet (*20*) generates a magnetic field gradient that results in distinct ESR transition frequencies for the left and right qubits. Electrically driven single-qubit rotations are implemented by "shaking" the electron spins in the transverse field gradient of the micromagnet (*7*, *21*). Other Si/SiGe device designs have suffered from accidental quantum dot

[1]Department of Physics, Princeton University, Princeton, NJ 08544, USA. [2]Department of Physics, University of Konstanz, D-78457 Konstanz, Germany. [3]Joint Quantum Institute and Joint Center for Quantum Information and Computer Science, NIST and University of Maryland, College Park, MD 20742, USA. [4]Research Center for Advanced Science and Technology, University of Tokyo, Tokyo, Japan.
*Corresponding author. Email: petta@princeton.edu

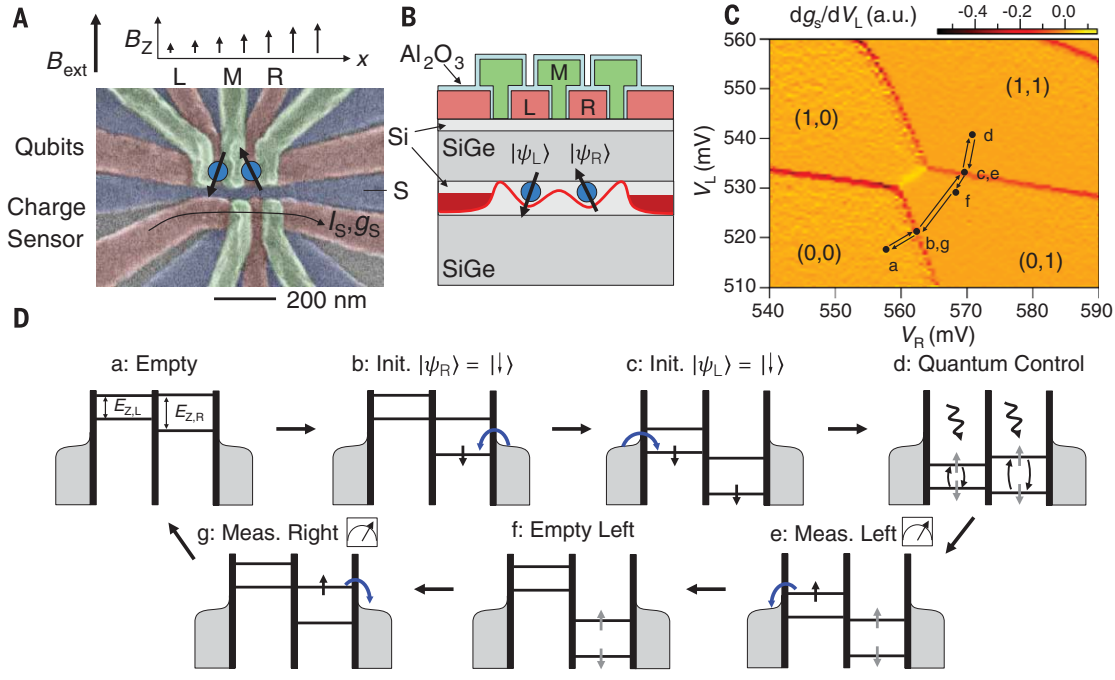

Fig. 1. Two-qubit device. (**A**) False-color scanning electron microscope image of the DQD before deposition of the Co micromagnet. Two spin qubits are defined by the DQD and a neighboring quantum dot is used as a charge sensor. The Co micromagnet (not shown) creates a slanting Zeeman field that is used for quantum control (upper schematic). (**B**) Schematic cross section of the DQD device. Two electrons are trapped in the confinement potential created by gates L, M, and R, to which voltages V_L, V_M, and V_R are applied, respectively. (**C**) DQD charge stability diagram. Points a to g are used in the two-qubit control sequence. (**D**) DQD energy level configuration at each point in the pulse sequence. Points a to c are used to initialize the system in $|\downarrow\downarrow\rangle$. Single-qubit and two-qubit gates are implemented at point d. Sequential single-shot spin state readout is achieved by navigating from point e to point g.

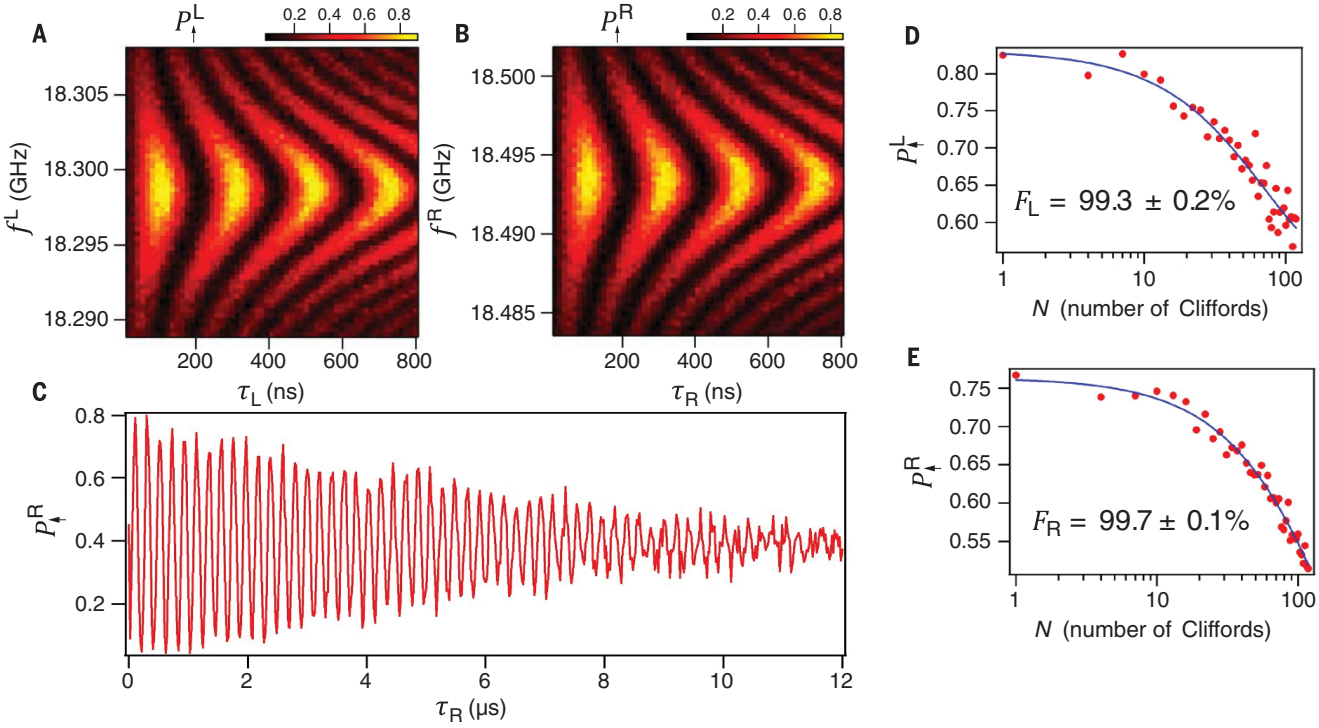

Fig. 2. High-fidelity single-qubit gates. (**A**) Left-qubit spin-up probability $P^L_\uparrow$ plotted as a function of the MW drive frequency f^L and drive time τ_L, showing coherent Rabi oscillations. (**B**) Right-qubit Rabi oscillations. (**C**) $P^R_\uparrow$ as a function of τ_R, obtained at a drive frequency f^R = 18.493 GHz, shows high-visibility Rabi oscillations that persist to 10 μs. (**D** and **E**) Clifford randomized benchmarking (*20*) of the left (D) and right (E) qubits yields gate fidelities F_L and F_R in excess of 99%.

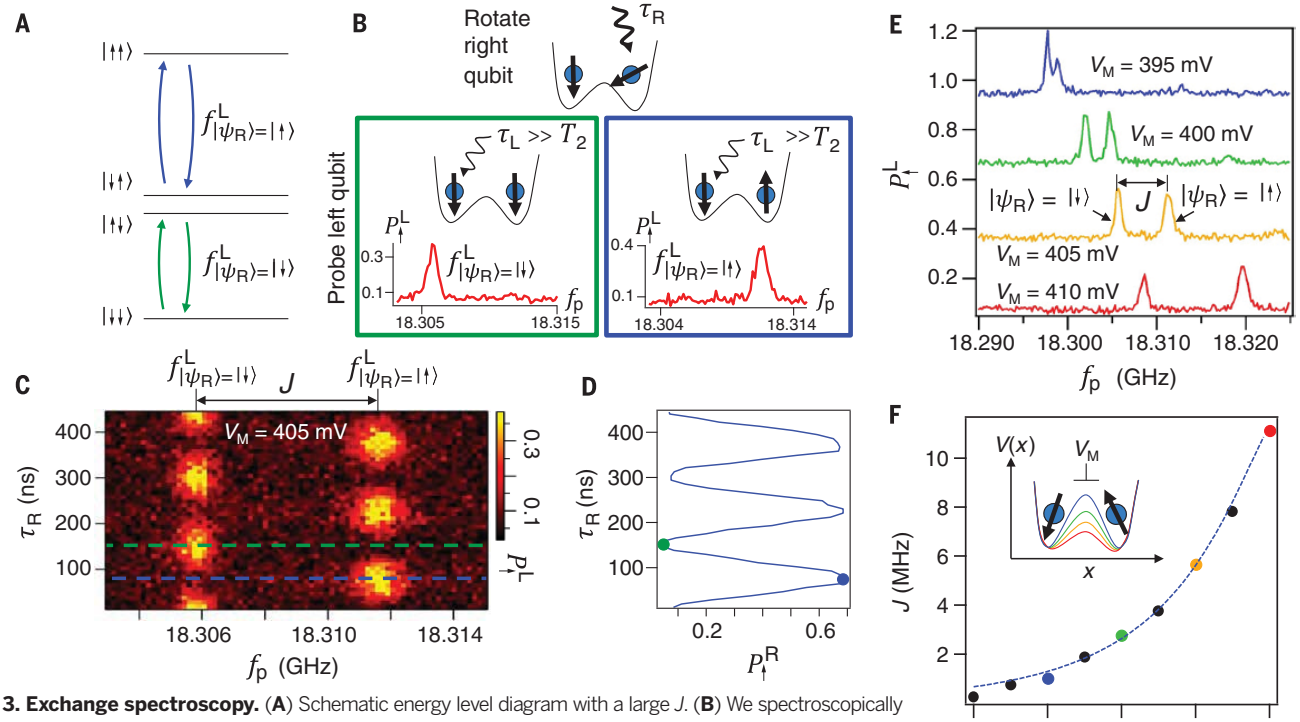

Fig. 3. Exchange spectroscopy. (**A**) Schematic energy level diagram with a large J. (**B**) We spectroscopically measure J by first applying a rotation to the right qubit and then applying a low-power probe tone to the left qubit. The left qubit will have a resonance frequency $f^L_{|\psi_R\rangle=|\downarrow\rangle}$ when the right qubit is in the spin-down state (green box) and $f^L_{|\psi_R\rangle=|\uparrow\rangle}$ when the right qubit is in the spin-up state (blue box). (**C**) $P^L_\uparrow$ as a function of τ_R and probe frequency f_p. The two resonance frequencies of the left qubit are split by J. The response of the left qubit to the probe tone oscillates between these two frequencies as the right qubit oscillates between spin-up and spin-down. (**D**) $P^R_\uparrow$ as a function of τ_R, displaying Rabi oscillations. (**E**) Spectra showing the left-dot resonance frequencies for four different values of V_M. Curves are offset by 0.3 for clarity. (**F**) J as a function of V_M (dots) and theory predictions (line) from (*20*). The DQD potentials for the colored data points are schematically illustrated by the corresponding colored curves in the inset.

formation, which is in part caused by the high effective mass of electrons in Si and by gate designs that are much larger than the single-electron wave function (*22*). In our experiments, isolation and control of single electrons are made possible by an overlapping aluminum gate electrode architecture that provides tight electronic confinement in a largely disorder-free potential. Our devices allow exquisite control of single electrons and nearest-neighbor exchange coupling, with the potential to scale to at least nine dots in a linear array (*19*).

The DQD gate voltages V_L and V_R are tuned to traverse the charge stability diagram. Starting from the charge state (N_L = 0, N_R = 0), where N_L and N_R respectively refer to the number of electrons in the left and right dots, we navigate from point a to point c in the stability diagram (Fig. 1C) to initialize the device in the $|\downarrow_L\downarrow_R\rangle$ state. The gates are then pulsed to point d, in the (1, 1) charge state, where single-qubit control is achieved by applying MW pulses to gate S. Exchange can be rapidly turned on and off (on a 5-ns time scale) by adjusting the voltage V_M. Qubit readout is achieved by moving from point e to point g, where the left and right dot spins are sequentially measured and emptied. Spin-dependent tunneling and charge state readout are used to extract the spin-up probabilities $P_\uparrow^L$ and $P_\uparrow^R$ of the left and right qubits, respectively, following references (*23*, *24*). Energy level diagrams corresponding to each point in the pulse sequence are shown in Fig. 1D. High-fidelity single-qubit control is demonstrated in Fig. 2, where randomized benchmarking yields single-qubit fidelities F_L = 99.3 ± 0.2% and F_R = 99.7 ± 0.1%.

Proposals for two-qubit interactions with spins in semiconductors are generally based on control of the exchange coupling (*18*). To implement a high-fidelity CNOT gate, we must first measure J as a function of V_M (*20*). Physically, in the presence of a strong magnetic field gradient $\delta B >> J$, the exchange interaction lowers the energy of the antiparallel spin states relative to the $|\uparrow\uparrow\rangle$ and $|\downarrow\downarrow\rangle$ spin states (Fig. 3A). As a result, the ESR frequency of the left qubit will be dependent on the state of the right qubit, and vice versa. We can therefore determine J by measuring the left-qubit ESR spectra for different right-qubit states (Fig. 3B). Specifically, the system is prepared in $|\downarrow\downarrow\rangle$ and then a rotation of duration τ_R is applied to the right qubit. Next, we apply a low-power probe tone for a time $\tau_L >> T_2$ at a frequency f_p that will leave the qubit in a mixed state if f_p is resonant with the qubit frequency. For the simple case where τ_R is such that the right qubit ends in the spin-down state, the left qubit will have a transition frequency $f^L_{|\psi_R\rangle=|\downarrow\rangle}$; likewise, when the right qubit ends in the spin-up state, the left qubit's transition frequency will be $f^L_{|\psi_R\rangle=|\uparrow\rangle}$ (Fig. 3B, green and blue boxes, respectively). By plotting $P_\uparrow^L$ as a function of τ_R and f_p (Fig. 3C), we see that the left-qubit resonance frequency is correlated with the state of the right qubit (Fig. 3D). The exchange frequency $J/h = f^L_{|\psi_R\rangle=|\uparrow\rangle} - f^L_{|\psi_R\rangle=|\downarrow\rangle}$, where h is Planck's constant, is directly extracted from the data sets in Fig. 3E and plotted as a function of V_M in Fig. 3F (*20*). A 20-mV change in V_M is sufficient to turn on an exchange interaction of 10 MHz, which exceeds typical single-qubit Rabi frequencies (f_{Rabi} = 4.8 MHz in Fig. 2C).

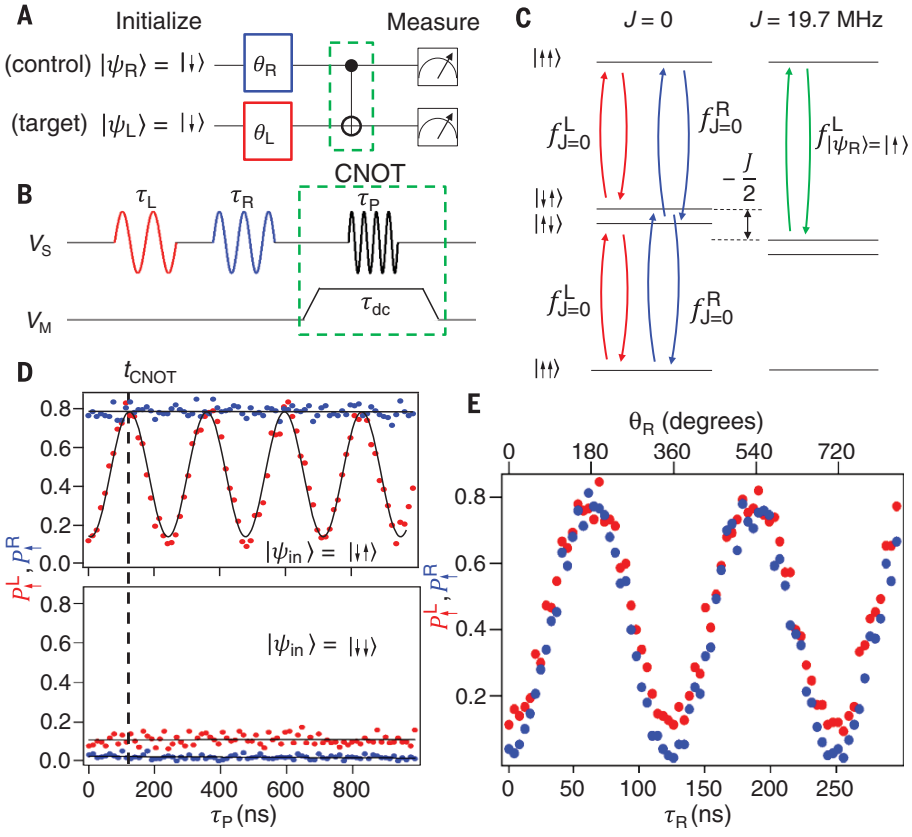

Fig. 4. CNOT gate. (**A**) Quantum circuit for the CNOT gate. (**B**) Experimental implementation of the quantum circuit. (**C**) Schematic energy level diagrams for $J = 0$ (left) and $J \neq 0$ (right). When $J \neq 0$, a conditional rotation can be applied to the left qubit by driving at $f^L_{|\psi_R\rangle=|\uparrow\rangle}$. (**D**) $P_\uparrow^L$ (red) and $P_\uparrow^R$ (blue) as a function of τ_P for input states $|\downarrow\uparrow\rangle$ (top) and $|\downarrow\downarrow\rangle$ (bottom). The vertical dashed line at τ_P = 130 ns = t_{CNOT} corresponds to a CNOT gate. (**E**) CNOT gate with superposition input states. With τ_P = 130 ns and τ_L = 0, the response of the CNOT gate is plotted as a function of τ_R, showing that the target qubit follows the state of the control qubit.

Fast gate voltage control of J can be used to implement a resonant CNOT gate (Fig. 4). The general quantum circuit and its experimental implementation are shown in Fig. 4, A and B. When V_M is low, J is approximately zero (J ~ 300 kHz for V_M = 390 mV; see Fig. 3F), corresponding to the level diagram at the left in Fig. 4C (*20*). With J ~ 0, high-fidelity single-qubit gates can be implemented, because the resonance frequency of each qubit is independent of the state of the other qubit (see Fig. 2). When V_M is pulsed high, the antiparallel spin states are lowered in energy by $J/2$ relative to the parallel spin states (Fig. 4C, right). In this configuration, the CNOT gate is resonantly implemented by driving the $|\downarrow\uparrow\rangle$ to $|\uparrow\uparrow\rangle$ transition. Here, $|tc\rangle$ describes a product state of the target (t) and control (c) qubits. In contrast, the $|\uparrow\downarrow\rangle$ to $|\downarrow\downarrow\rangle$ transition is off-resonant as a result of the J coupling, allowing for a conditional rotation that is dependent on the right electron's spin state.

To calibrate the CNOT gate, we use a long direct-current exchange pulse of length τ_{dc} = 1 μs and vary the length τ_P of the MW pulse to drive transitions between $|\downarrow\uparrow\rangle$ and $|\uparrow\uparrow\rangle$. The resulting conditional oscillations are shown in Fig. 4D for the input states $|\downarrow\uparrow\rangle$ and $|\downarrow\downarrow\rangle$. A conditional π-rotation is realized on the target qubit for $t_{CNOT} = \tau_P$ = 130 ns. Thanks to the magnetic field gradient, changes in V_M shift the orbital positions of the electrons and result in small changes in the ESR resonance frequencies. By setting $\tau_{dc} = 2\pi/J$ = 204 ns, we eliminate conditional phases caused by exchange and the remaining single-qubit phases are accounted for in the phase of the consecutive MW drives, resulting in a pure CNOT gate (*20*). In contrast to our single-step CNOT gate, implementation of a conventional CNOT gate following the Loss-DiVincenzo proposal would require mastery of two $\sqrt{\text{SWAP}}$ operations and three single-qubit gates (*18*).

In general, the CNOT gate must be able to operate on an arbitrary input state, and specifically on product states of the form

$$|\psi_{in}\rangle = (\alpha_L|\downarrow\rangle_L + \beta_L|\uparrow\rangle_L) \otimes (\alpha_R|\downarrow\rangle_R + \beta_R|\uparrow\rangle_R) \quad (1)$$

where R and L denote the right (control) and left (target) qubits. Here, $|\alpha_{L,R}|^2 + |\beta_{L,R}|^2 = 1$. To test the basic functionality of the CNOT gate, we

first initialize the system in $|\downarrow\downarrow\rangle$. The control qubit is then rotated by an angle θ_R to create the input state

$$|\psi_{in}\rangle = |\downarrow\rangle_L \otimes \left[\cos\left(\frac{\theta_R}{2}\right)|\downarrow\rangle_R - i\sin\left(\frac{\theta_R}{2}\right)|\uparrow\rangle_R\right] \quad (2)$$

Figure 4E shows $P_\uparrow^L$ and $P_\uparrow^R$ measured after the CNOT gate acts on different input states with angle θ_R. These data show that the CNOT acts as expected on states outside of the classical set of (product) input states $|\uparrow\uparrow\rangle$, $|\uparrow\downarrow\rangle$, $|\downarrow\uparrow\rangle$, and $|\downarrow\downarrow\rangle$ and that the control qubit is not flipped during the CNOT operation.

We next use the CNOT gate (*20*) to create the Bell state $|\psi_{target}\rangle = \frac{1}{\sqrt{2}}(|\downarrow\downarrow\rangle - i|\uparrow\uparrow\rangle)$ and extract its fidelity by performing two-qubit state tomography (*25*, *26*). The Bell state is created by initializing the system in $|\downarrow\downarrow\rangle$ and applying a $\pi/2_x$ pulse on the control spin, which generates the input state $|\psi_{in}\rangle = \frac{1}{\sqrt{2}}(|\downarrow\downarrow\rangle - i|\downarrow\uparrow\rangle)$. Application of the CNOT gate to $|\psi_{in}\rangle$ yields $|\psi_{target}\rangle = \frac{1}{\sqrt{2}}(|\downarrow\downarrow\rangle - i|\uparrow\uparrow\rangle)$. State tomography is performed by appending single-qubit rotations after the CNOT gate to measure the expectation value for all two-qubit Pauli operators (for example, by applying a $\pi/2_x$ rotation to the left qubit and $\pi/2_y$ rotation to the right qubit, we measure the YX two-qubit operator). Because the set of Pauli operators forms a basis of the Hermitian operators on the two-qubit Hilbert space, we can reconstruct the full two-qubit density matrix from these measurements. Not accounting for imperfections in state preparation and measurement (SPAM), we obtain a fidelity $F_{raw} = \langle\psi_{target}|\rho|\psi_{target}\rangle = 56\%$ (*27*). The readout visibilities of both qubits (*20*) and spin relaxation during the sequential qubit readout together account for a considerable amount of the infidelity. By adopting the procedure used in (*22*), we correct our density matrix to account for SPAM errors and obtain a corrected fidelity $F = \langle\psi_{target}|\rho|\psi_{target}\rangle = 78\%$. We anticipate that the state fidelity can be further improved through the use of optimized pulse sequences (*28*).

Realizing robust two-qubit gates has been a bottleneck in the development of spin-based quantum computers (*12*, *29*). By combining our results with recent advances in Si/SiGe quantum dot device technology (*19*), we anticipate that it will become feasible to demonstrate nine-qubit quantum processors in silicon.

REFERENCES AND NOTES

1. R. Hanson, L. P. Kouwenhoven, J. R. Petta, S. Tarucha, L. M. K. Vandersypen, *Rev. Mod. Phys.* **79**, 1217–1265 (2007).
2. F. A. Zwanenburg *et al.*, *Rev. Mod. Phys.* **85**, 961–1019 (2013).
3. M. Veldhorst *et al.*, *Nat. Nanotechnol.* **9**, 981–985 (2014).
4. M. Steger *et al.*, *Science* **336**, 1280–1283 (2012).
5. A. M. Tyryshkin *et al.*, *Nat. Mater.* **11**, 143–147 (2011).
6. M. Pioro-Ladrière *et al.*, *Nat. Phys.* **4**, 776–779 (2008).
7. Y. Tokura, W. G. van der Wiel, T. Obata, S. Tarucha, *Phys. Rev. Lett.* **96**, 047202 (2006).
8. J. P. Dehollain *et al.*, *New J. Phys.* **18**, 103018 (2016).
9. J. Yoneda, K. Takeda, T. Otsuka, T. Nakajima, M. R. Delbecq, G. Allison, T. Honda, T. Kodera, S. Oda, Y. Hoshi, N. Usami, K. M. Itoh, S. Tarucha, arXiv:1708.01454 (2017).
10. J. R. Petta *et al.*, *Science* **309**, 2180–2184 (2005).
11. K. C. Nowack *et al.*, *Science* **333**, 1269–1272 (2011).
12. R. Brunner *et al.*, *Phys. Rev. Lett.* **107**, 146801 (2011).
13. M. D. Shulman *et al.*, *Science* **336**, 202–205 (2012).
14. M. Veldhorst *et al.*, *Nature* **526**, 410–414 (2015).
15. F. Martins *et al.*, *Phys. Rev. Lett.* **116**, 116801 (2016).
16. M. D. Reed *et al.*, *Phys. Rev. Lett.* **116**, 110402 (2016).
17. B. Bertrand *et al.*, *Phys. Rev. Lett.* **115**, 096801 (2015).
18. D. Loss, D. P. DiVincenzo, *Phys. Rev. A* **57**, 120–126 (1998).
19. D. M. Zajac, T. M. Hazard, X. Mi, E. Nielsen, J. R. Petta, *Phys. Rev. Appl.* **6**, 054013 (2016).
20. See supplementary materials.
21. E. Kawakami *et al.*, *Nat. Nanotechnol.* **9**, 666–670 (2014).
22. T. F. Watson, S. G. J. Philips, E. Kawakami, D. R. Ward, P. Scarlino, M. Veldhorst, D. E. Savage, M. G. Lagally, M. Friesen, S. N. Coppersmith, M. A. Eriksson, L. M. K. Vandersypen, arXiv:1708.04214 (2017).
23. J. M. Elzerman *et al.*, *Nature* **430**, 431–435 (2004).
24. A. Morello *et al.*, *Nature* **467**, 687–691 (2010).
25. M. Steffen *et al.*, *Science* **313**, 1423–1425 (2006).
26. Y. X. Liu, L. F. Wei, F. Nori, *Phys. Rev. B* **72**, 014547 (2005).
27. M. A. Nielsen, I. L. Chuang, *Quantum Computation and Quantum Information* (Cambridge Univ. Press, 2000).
28. M. Russ, D. M. Zajac, A. J. Sigillito, F. Borjans, J. M. Taylor, J. R. Petta, G. Burkard, arXiv:1711.00754 (2017).
29. Shortly after the submission of our results, another group reported exchange coupling in a Si/SiGe double quantum dot (*22*).

ACKNOWLEDGMENTS

We thank T. Hazard, J. Stehlik, and K. Wang for technical assistance. Research was sponsored by Army Research Office grant W911NF-15-1-0149, the Gordon and Betty Moore Foundation's EPiQS Initiative through grant GBMF4535, and NSF grant DMR-1409556. Devices were fabricated in the Princeton University Quantum Device Nanofabrication Laboratory. Any mention of commercial products is for information only; it does not imply recommendation or endorsement by NIST. The data that support the findings of this study are available in the supplementary materials. Additional data can be obtained from the corresponding author upon request.

SUPPLEMENTARY MATERIALS

www.sciencemag.org/content/359/6374/439/suppl/DC1
Materials and Methods
Supplementary Text
Figs. S1 to S10
References (*30*–*40*)

7 August 2017; accepted 28 November 2017
Published online 7 December 2017
10.1126/science.aao5965

Science

Resonantly driven CNOT gate for electron spins

D. M. Zajac, A. J. Sigillito, M. Russ, F. Borjans, J. M. Taylor, G. Burkard and J. R. Petta

Science **359** (6374), 439-442.
DOI: 10.1126/science.aao5965originally published online December 7, 2017

Building an essential quantum component

To build a universal quantum computer—the kind that can handle any computational task you throw at it—an essential early step is to demonstrate the so-called CNOT gate, which acts on two qubits. Zajac *et al.* built an efficient CNOT gate by using electron spin qubits in silicon quantum dots, an implementation that is especially appealing because of its compatibility with existing semiconductor-based electronics (see the Perspective by Schreiber and Bluhm). To showcase the potential, the authors used the gate to create an entangled quantum state called the Bell state.

Science, this issue p. 439; see also p. 393